



Minerva Access is the Institutional Repository of The University of Melbourne

Author/s:

Tsurugizawa, T; Tamada, K; Ono, N; Karakawa, S; Kodama, Y; Debacker, C; Hata, J; Okano, H; Kitamura, A; Zalesky, A; Takumi, T

Title:

Awake functional MRI detects neural circuit dysfunction in a mouse model of autism

Date:

2020-02-05

Citation:

Tsurugizawa, T., Tamada, K., Ono, N., Karakawa, S., Kodama, Y., Debacker, C., Hata, J., Okano, H., Kitamura, A., Zalesky, A. & Takumi, T. (2020). Awake functional MRI detects neural circuit dysfunction in a mouse model of autism. *Science Advances*, 6 (6), <https://doi.org/10.1126/sciadv.aav4520>.

Persistent Link:

<https://hdl.handle.net/11343/245620>

License:

[CC BY-NC](#)

NEUROSCIENCE

Awake functional MRI detects neural circuit dysfunction in a mouse model of autism

Tomokazu Tsurugizawa^{1*}, Kota Tamada², Nobukazu Ono³, Sachise Karakawa³, Yuko Kodama³, Clement Debacker¹, Junichi Hata^{2,4}, Hideyuki Okano^{2,4}, Akihiko Kitamura³, Andrew Zalesky⁵, Toru Takumi^{2,6*}

MRI has potential as a translational approach from rodents to humans. However, given that mouse functional MRI (fMRI) uses anesthetics for suppression of motion, it has been difficult to directly compare the result of fMRI in “unconsciousness” disease model mice with that in “consciousness” patients. We develop awake fMRI to investigate brain function in *15q dup* mice, a copy number variation model of autism. Compared to wild-type mice, we find that *15q dup* is associated with whole-brain functional hypoconnectivity and diminished fMRI responses to odors of stranger mice. Ex vivo diffusion MRI reveals widespread anomalies in white matter ultrastructure in *15q dup* mice, suggesting a putative anatomical substrate for these functional hypoconnectivity. We show that D-cycloserine (DCS) treatment partially normalizes these anomalies in the frontal cortex of *15q dup* mice and rescues some social behaviors. Our results demonstrate the utility of awake rodent fMRI and provide a rationale for further investigation of DCS therapy.

INTRODUCTION

Autism spectrum disorder (ASD) is a common and heterogeneous disorder characterized by deficits in social interaction and communication and restricted repetitive patterns of behavior, interest, and activities. Human genetics and animal model studies for ASD have rapidly progressed (1). Among the etiology of ASD, copy number variation (CNV) is a well-known cause (2), and a mouse model for human 15q11-13 duplication (*15q dup*) is the first CNV mouse model of ASD (3). It is established that *15q dup* mice display abnormal behavior resembling ASD symptoms; poor social interaction, behavioral inflexibility, abnormal ultrasonic vocalizations (USVs), and correlates of anxiety (3, 4). They also exhibit altered spine dynamics (5) and impaired excitatory/inhibitory balance (6) in the cerebral cortex, as well as long-term depression dysregulation and abnormal synaptic pruning in the cerebellum (7). In addition to these phenotypes, *15q dup* mice show loss of gray matter volume relative to wild-type (WT) mice in several regions, including the hypothalamus, thalamus, inferior/superior colliculus, midbrain, and pons (8). Given the widespread gray matter atrophy and altered spine dynamics in *15q dup* mice, we hypothesized that these genetically altered mice would show corresponding alterations in resting-state functional connectivity and white matter ultrastructure, such as frontoparietal lobe and bilateral cortices.

Recent studies reveal that D-cycloserine (DCS), a D-serine analog, is effective in ameliorating autistic-like behavior or electrophysiological alterations associated with ASD (9). DCS may impart a regulatory effect on N-methyl-D-aspartate (NMDA) hypofunction in ASD on the mammalian target of rapamycin activity, potentially resulting in the observed improvement in sociability. However, trials evaluating DCS provide varying levels of evidence of efficacy (10), and it

remains unclear whether the prosocial effects of DCS are accompanied by normalization of ASD-related functional connectivity deficits. We hypothesized that DCS would normalize aberrant networks of resting-state functional connectivity in *15q dup* mice, particularly connections to the frontal cortices. Investigating these hypotheses in ASD model mice remains challenging due to the difficulty in performing functional magnetic resonance imaging (fMRI) in awake rodents. To address this challenge, we developed an awake fMRI protocol for mice and used this technique to study the functional effect of DCS on *15q dup* mice.

While human fMRI is ubiquitous and a promising tool to investigate brain function noninvasively, mouse fMRI provides an important translational tool to bridge the gap between invasive research in disease model animals and clinical research in patients. However, compared to human fMRI, mouse fMRI is limited by the need for anesthesia to suppress body motion during fMRI scanning. Performing mouse fMRI studies under light anesthesia can ameliorate body motion (11), but it remains unclear whether this light anesthesia (11, 12) provides a reasonable characterization of a completely “awake” state of consciousness throughout acquisition of resting-state fMRI (rsfMRI) or task-based fMRI in rodents (13–17). Awake mouse fMRI can therefore provide a fundamental technique to understand the link between circuits and behavior. In this study, combined with careful acclimation training and gentle fixation, we developed an awake mouse fMRI system without anesthetics to investigate alterations in brain function in *15q dup* mice. We conducted two awake fMRI paradigms; rsfMRI and task-based fMRI with other-odorant stimulation as a cognitive task because odor discrimination is an essential factor in social interaction in mice. Furthermore, we assessed whether DCS can improve sociability and normalize any potential deficits in brain function and activation in awake *15q dup* mice.

RESULTS

Physiological measurements, head motion, and electroencephalography

To enable fMRI acquisition in awake mice, we developed an apparatus for head immobilization, which comprised a head bar that was

Copyright © 2020 The Authors, some rights reserved; exclusive licensee American Association for the Advancement of Science. No claim to original U.S. Government Works. Distributed under a Creative Commons Attribution NonCommercial License 4.0 (CC BY-NC).

¹NeuroSpin, Commissariat à l’Energie Atomique et aux Energies Alternatives, CEA Saclay, Gif-sur-Yvette 91191, France. ²RIKEN Brain Science Institute, Wako, Saitama 351-0198, Japan. ³Institute for Innovation, Ajinomoto Co. Inc., Kawasaki 210-8681, Japan. ⁴Department of Physiology, Keio University School of Medicine, Shinjuku, Tokyo 160-8585, Japan. ⁵Melbourne Neuropsychiatry Centre and Department of Biomedical Engineering, University of Melbourne, Victoria 3010, Australia. ⁶Department of Physiology and Cell Biology, Kobe University School of Medicine, Chuo, Kobe 650-0017, Japan. *Corresponding author. Email: tsurugizawa@gmail.com (T.Ts.); takumit@med.kobe-u.ac.jp (T.Ta.)

cemented to the animal's skull and securely affixed to a head fixation frame (fig. S1, A and B). The immobilization apparatus physically restricted the potential for head movement along all planes. Mice were subjected to 4 days of training before the fMRI acquisition to acclimate to the head bar and fMRI setup, as acclimatization training minimizes acclimation training minimizes stress and anxiety during the acquisition interval (fig. S1C). To verify that adequate acclimation was achieved, we monitored three key physiological measures after each day of acclimation training. Daily monitoring showed that (i) heart rate was abnormally elevated on the first day of training, most likely indicating increased stress levels, but reduced to normal levels on the fourth day (fig. S1D); (ii) respiration rate did not significantly change across four training days (fig. S1E), consistent with a previous study (18); and (iii) serum corticosterone levels, which provide an index of stress levels, were significantly elevated compared to levels without head immobilization but decreased to normal levels on the last days of acclimation training (fig. S1F). Normalization of these physiological measures by the end of training suggested that adequate acclimation to the head immobilization apparatus was achieved. There was no significant difference in the respiratory rate and heart rate between WT and *15q dup* groups (fig. S1G), indicating that acclimation training was also achieved in *15q dup* mice.

Light anesthesia (isoflurane) was administered to enable cementation of the head bar and MRI shimming. The fMRI acquisition commenced 10 min after cessation of isoflurane delivery. To ensure that 10 min was adequate for the effects of isoflurane to dissipate, we performed electroencephalography (EEG) on the frontal cortex throughout this 10-min interval, which indicated that the power of gamma frequency oscillations significantly increased after cessation of isoflurane delivery (fig. S2). We continuously observed EEG until 30 min after cessation of isoflurane with two mice, and the gamma EEG was similar to that at 10 min. This suggested the dissipation of anesthesia effects (19). Furthermore, the heart rate increased from >150 to >450 beats/min in 10 min following cessation of isoflurane delivery. This is consistent with a previous work suggesting that 10 min is sufficient to recover from light isoflurane anesthesia, and blood isoflurane is cleaned in 8 min (16). Finally, we sought to verify that our head immobilization apparatus adequately suppressed any potential intrascan head movement. To this end, potential head movement associated with each fMRI volume was parameterized in terms of six displacement and rotation parameters (see Materials and Methods). Figure S3A shows these parameters for a representative animal. Given that the head bar was securely coupled to the head positioning apparatus (fig. S1, A and B), head motion was severely constrained along all planes from the first day of MRI training (fig. S3B).

Resting-state functional connectivity in WT and *15q dup* mice

We used our awake mouse fMRI system to investigate differences in resting-state functional connectivity between WT and *15q dup*-saline mice. To provide a whole-brain characterization of resting-state functional connectivity, the cortex was parcellated into 32 broad regions, and the Pearson correlation coefficient was measured between pairs of regionally averaged fMRI time series to yield a 32×32 connectivity matrix for each mouse (Fig. 1A). This matrix quantified the strength of functional connectivity between 496 distinct pairs of regions. The network-based statistic (NBS) (20) was used to identify pairs of regions for which functional connectivity strength significantly differed between WT and *15q dup* groups while controlling the familywise error rate. Hypoconnectivity in the *15q dup* group

was evident in a widespread subnetwork that spanned all regions and a majority of connections (Fig. 1, B and C). The most extensive reductions in connectivity strength according to the effect size were observed in the hindbrain [pons, dorsal raphe nucleus (DRN), and regions including lateral parabrachial nucleus (LPBN)/locus coeruleus (LC)], thalamic nuclei (ThN), caudate putamen (CPu), and motor cortex (MC) (Fig. 1D). No evidence of hyperconnectivity was found in the *15q dup* group. Last, we sought to assess the test-retest reproducibility of the functional connectivity matrices mapped with our awake mouse fMRI system. To this end, two separate fMRI acquisitions for each of five WT mice were acquired across consecutive days, resulting in a total of 10 datasets. A connectivity matrix was mapped for each dataset, and the correlation between corresponding pairs of matrices was computed. This yielded a Pearson correlation coefficient of 0.92 ± 0.01 , indicating excellent test-retest reproducibility.

Odor stimulation in WT and *15q dup* mice

To investigate odor response in the *15q dup* group, we augmented the awake mouse fMRI system to deliver odor stimulation using a dedicated nasal mask (Fig. 2, A to C). Excretions from stranger mice were used to generate the odor. First, we confirmed that odor stimulation evoked BOLD (blood oxygenation level-dependent) responses in the olfactory bulb, including the superior and lateral glomerular layer of the olfactory bulb (fig. S4, A to C), which is known to be activated by odor stimulation (21). Within the olfactory bulb and cortex, we did not find a significant difference in odor-evoked BOLD response between WT and *15q dup* groups. In the whole brain, the WT group showed a significant odor stimulation-evoked BOLD response in several regions including the hippocampus, ThN, hypothalamus, LC/LPBN, pons, and the cerebellum (Fig. 2D). In contrast, the BOLD response in these regions did not significantly increase in the *15q dup* group compared with the WT group (Fig. 2, D and E). There was no significant change in the respiratory rate and head motion during odor stimulation.

Diffusion tensor imaging in WT and *15q dup* mice

In parallel to the fMRI study, mice were euthanized, and diffusion tensor imaging (DTI) was performed on fixed brain tissue. Fractional anisotropy (FA) was assessed within each region of interest (ROI) to provide a generalized index of gray matter microstructure, which may characterize axonal loss and/or the effects of demyelination. This diffusion MRI index has long been used to successfully assess gray matter microstructure in both human MRI (22) and rodent MRI (23). No significant between-group difference in FA was found [$P > 0.05$, false discovery rate (FDR)], although FA in most of gray matter appeared lower in the *15q dup* group (Fig. 3A). Given this observation, we averaged FA across voxels comprising each of 16 gray matter regions, yielding regionally averaged FA estimates, with the aim of testing for regional gray matter demyelination or axon loss (24). These regionally averaged FA estimates were analyzed using a two-way analysis of variance (ANOVA), modeling the main effects of gray matter region (16 regions) and group (WT and *15q dup*) (Fig. 3B). The main effect of group was significant, with FA reduced in the *15q dup* group, but the interaction between region and group was not significant. This suggested that gray matter FA reductions in the *15q dup* group were diffuse and widespread, as opposed to being circumscribed to particular regions. We also compared structural connectivity [FA and edge weight (EW)] between the same groups (Fig. 3, C and D). Although there was no significant difference in

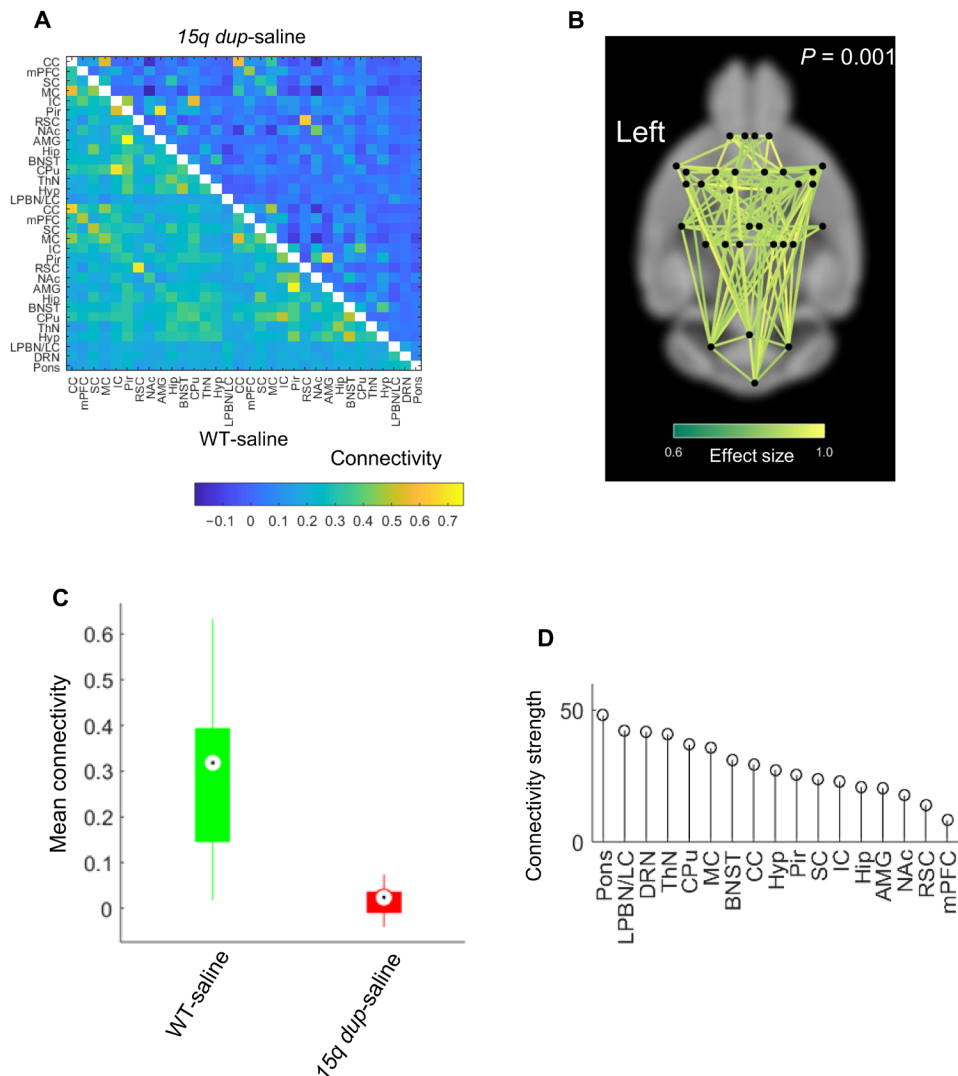


Fig. 1. NBS detect global hypoconnectivity in *15q dup* mice. (A) Group-averaged connectivity matrices (Pearson correlation coefficients) in WT-saline (bottom, $n = 15$) and *15q dup*-saline groups (top, $n = 10$). Color bar represents the Pearson correlation coefficient. (B) Network of reduced connectivity in the *15q dup*-saline group identified with the NBS ($P = 0.001$). Connections are colored according to effect size (Cohen's d). (C) Box plot showing distribution of network-averaged connectivity in WT-saline and *15q dup*-saline groups. Connectivity averaged over the connections comprising the network in (A). Circles indicate medians, and boxes indicate 25th and 75th percentiles. (D) Extent to which individual regions are affected by the network of reduced connectivity in the *15q dup* group. Strength is the sum of effects sizes across all connections associated with a given region. Strength is averaged between contralateral regions. CC, anterior cingulate cortex; mPFC, medial prefrontal cortex; SC, somatosensory cortex; IC, insular cortex; Pir, piriform; RSC, retrosplenial cortex; NAC, nucleus accumbens; AMG, amygdala; Hip, hippocampus; BNST, bed nucleus and stria terminus; Hyp, hypothalamus.

structural connectivity between WT and *15q dup* groups ($P > 0.05$ at FDR corrected), the averaged structural connectivity in *15q dup* mice was broadly smaller than WT mice.

L- and D-serine quantification in brain tissue

To investigate potential molecular factors that underlie the widespread reduced functional connectivity found in the *15q dup* group, we performed a comprehensive screening of amino acids in brain tissue. Concentrations of 30 amino acids were measured with liquid chromatography–tandem mass spectrometry (LC-MS/MS) analysis in three hindbrain and four forebrain regions (tables S1 and S2). For example, in agreement with a previous report (25), carnosine was found to be specific to the olfactory bulb, suggesting high quantification fidelity in our analysis. Concentrations of three amino acids significantly

differed between WT and *15q dup* groups (Fig. 4A). Compared with WT, taurine in the cerebellum and α -amino adipic acid in the frontal cortex were increased, while serine in the frontal cortex was decreased in the *15q dup* group. Since serine includes D and L forms and their functional roles are distinct, we examined concentrations of L- and D-serine at the postnatal developmental stage by using high-performance liquid chromatography (HPLC). At 1-week postnatal, a trend toward reduced concentrations of both D/L-serine was found in the *15q dup* group (Fig. 4, B and C), and the difference between WT and *15q dup* groups became significant at 3 weeks.

DCS treatment can rescue social behavior

DCS was administered to a subgroup of *15q dup* mice, while a comparison subgroup was administered saline. These mice are referred

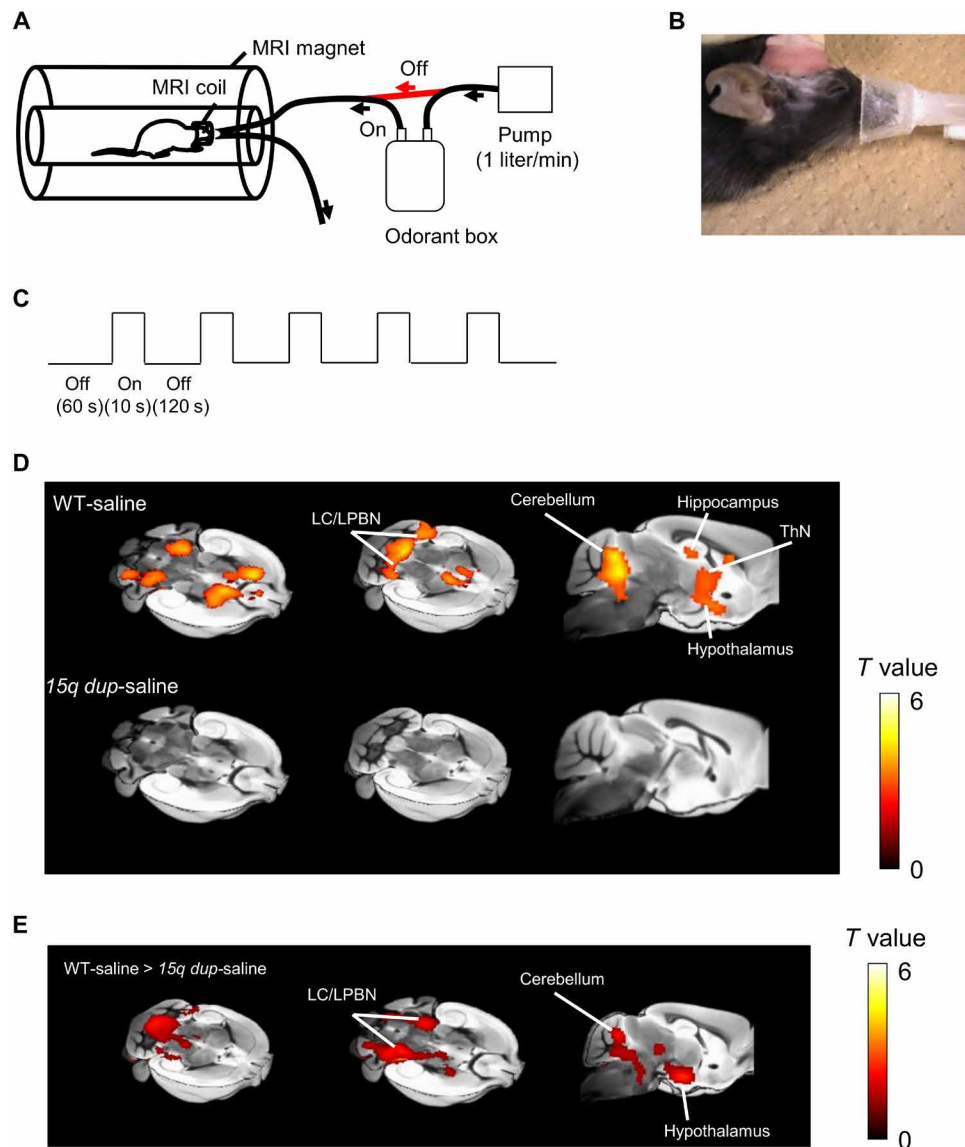


Fig. 2. Distinct BOLD response to odor stimulation between WT and *15q dup*-saline mice. (A) Schematic of odor presentation system. (B) Photo of dedicated mouse odor mask. (Photo credit: T. Tsurugizawa, Ajinomoto Co. Inc.) (C) Schedule of odor stimulation task. (D) Significant BOLD response to other-odor stimulation in WT-saline ($n = 15$) or *15q dup*-saline mice ($n = 10$; $P < 0.05$, false discovery rate (FDR)-corrected at the cluster level). (E) Significant BOLD response to other-odor stimulation in WT-saline compared to *15q dup*-saline ($P < 0.05$, FDR-corrected at the cluster level). Color bar represents the t statistic value.

to as *15q dup*-DCS and *15q dup*-saline. Similarly, WT mice were administered either DCS or saline. We assessed the acute effects of DCS treatment on autistic-like behavior, including reciprocal social interaction, female-induced USV, and correlates of anxiety. WT-saline and WT-DCS groups did not significantly differ in any behavioral tests, except for USV test (Fig. 4, D to F). In the reciprocal social interaction test, social interaction times were significantly decreased in the *15q dup*-saline group compared to the WT-saline group (Fig. 4D). An acute intraperitoneal injection of DCS restored this abnormal social interaction (Fig. 4D). On the other hand, DCS had no effect on the center time in the open-field test and the number of calls in USV, both of which were reduced in the *15q dup*-saline group, compared to the WT-saline group (Fig. 4, E and F). We therefore conclude that single acute DCS administration can ameliorate abnormal social interaction seen in *15q dup* mice.

Awake fMRI shows that DCS partially normalizes brain function

To evaluate the effect of DCS on functional connectivity, we performed rsfMRI and fMRI with odorant stimulation in *15q dup* mice administered DCS. The same protocols were also performed on *15q dup* mice administered saline to provide a comparison group. The NBS was used to test for differences in functional connectivity strength between the two groups across 496 distinct pairs of regions. DCS normalized functional connections between regions of the forebrain cortex ($P < 0.05$; Fig. 5A), although treatment did not normalize functional connectivity deficits that extended beyond the forebrain (Fig. 5B). Specifically, the normalizing effects of DCS were circumscribed to significant increases in connectivity between forebrain regions of the *15q dup*-DCS group, including the CPu, ThN, and hypothalamus, compared to the *15q dup*-saline group (Fig. 5C).

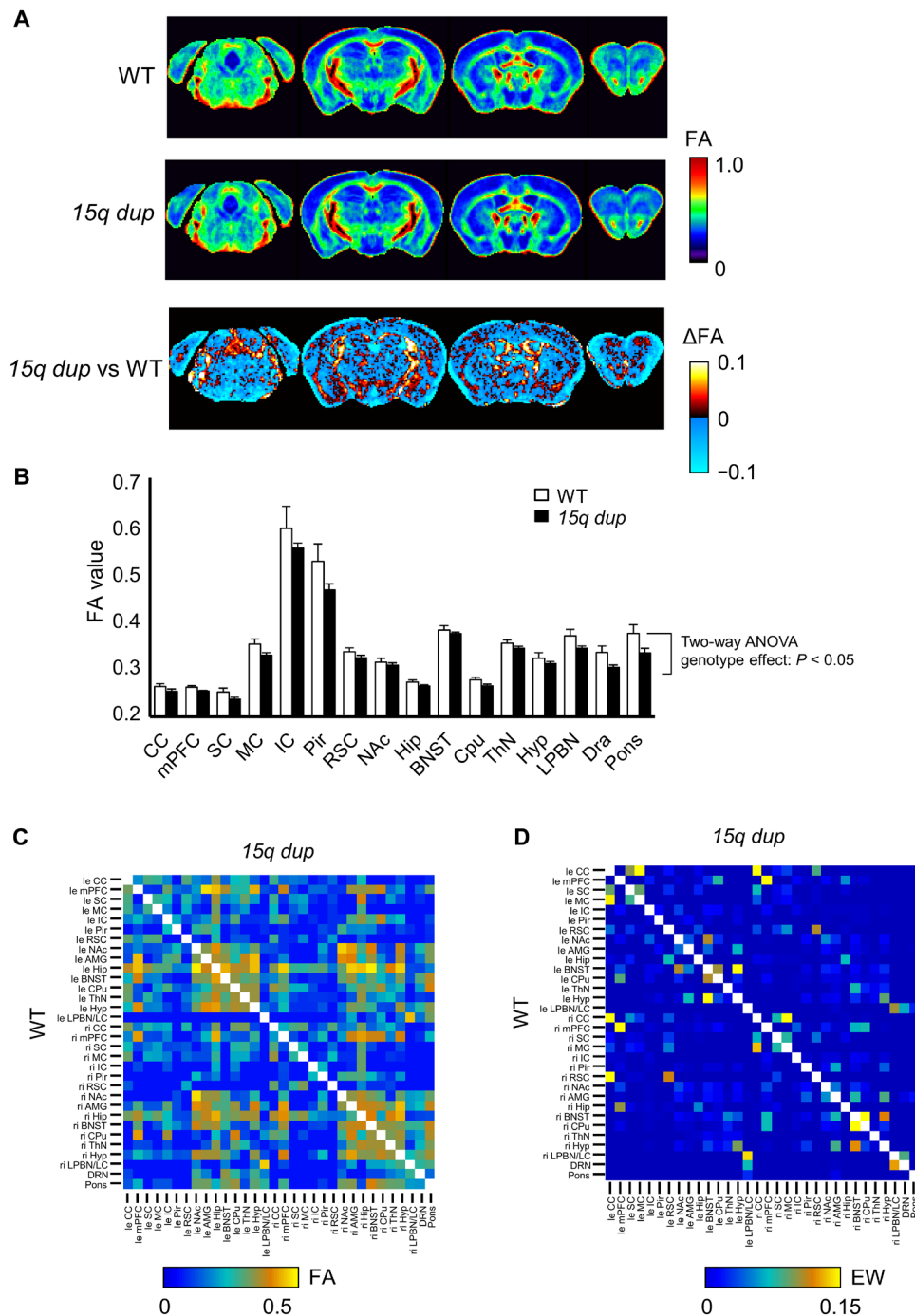


Fig. 3. FA and structural connectivity in 15q dup mice. (A) Group-averaged FA maps in WT (top, $n = 10$) and 15q dup mice (middle, $n = 12$) and differences of FA between WT and 15q dup groups (bottom). Color bar, FA value and Δ FA. (B) Averaged FA values within each ROI in WT ($n = 10$) and 15q dup mice ($n = 12$). (C) Mean FA and (D) EW structural connectivity in the same ROIs as functional connectivity in WT (bottom) and 15q dup (top) groups. Color bar, FA or EW.

With respect to functional connectivity averaged across this circumscribed network of connections, the mean connectivity in DCS-treated 15q dup mice was similar to that in WT-saline mice ($P > 0.05$; Fig. 5D). This suggests a putative mechanism for the prosocial effects of DCS that involves normalization of ASD-related hypoconnectivity, specifically within the forebrain subcortical regions. Despite this circumscribed normalization of forebrain functional connectivity

in the 15q dup-DCS group, extensive functional connectivity reductions remained after DCS administration (Fig. 5A). In supplementary investigations, dual-regression analysis (26, 27) was used to delineate the default mode network (DMN) based on associations between the retrosplenial cortex (RSC) and anterior cingulate cortex (CC) and a part of visual cortex and hippocampus. We found that functional connectivity in the DMN was significantly reduced in the 15q dup-saline

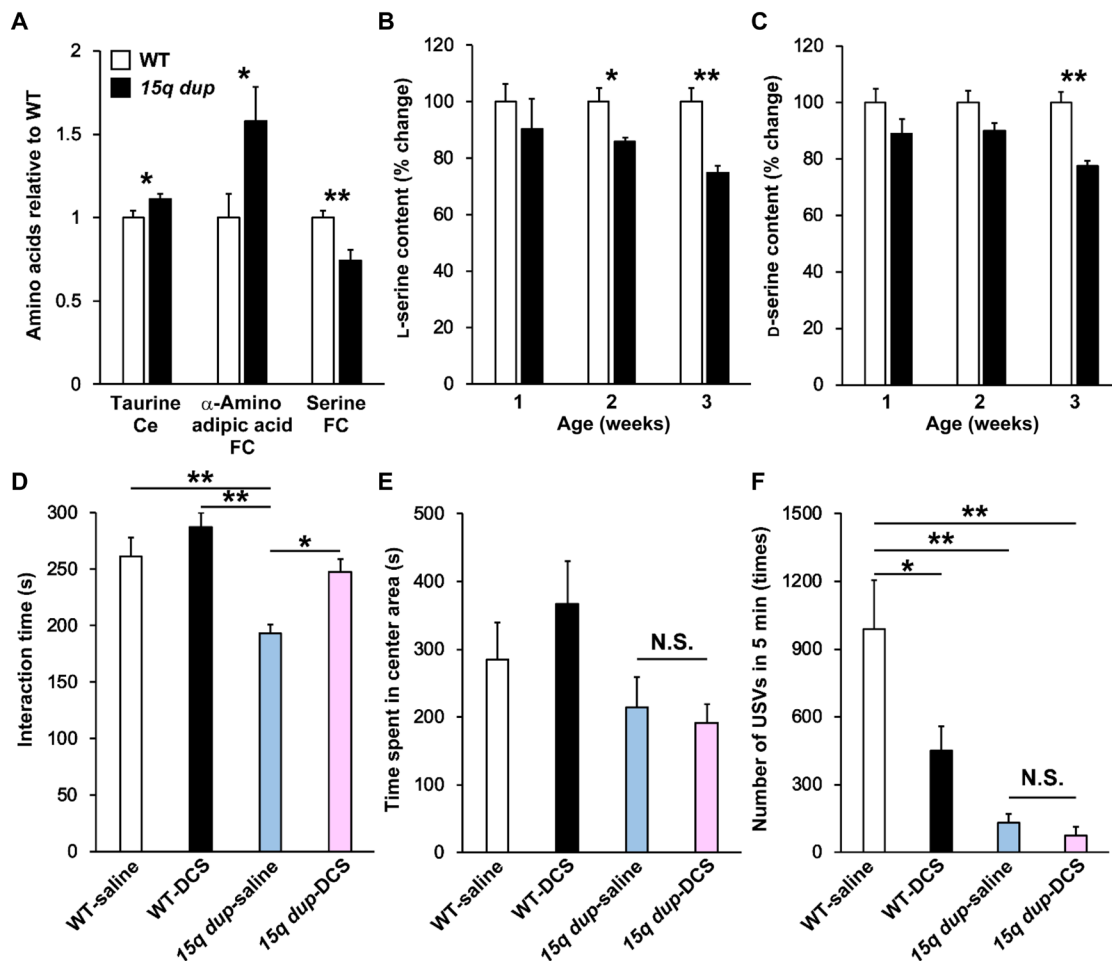


Fig. 4. Decreased brain serine and restored social behavior by acute DCS treatment in 15q dup mice. (A) Changes in amino acid concentrations between WT and 15q dup mice ($n = 6$ in each group). The mean level of WT-saline was set to 1. Ce, cerebellum; FC, frontal cortex. (B and C) Quantification of L- and D-serine concentrations in the frontal cortex. Mice that were 1 to 3 weeks postnatal were used for this analysis ($n = 4, 7,$ and 10 15q dup and $n = 9, 6,$ and 7 WT mice of ages 1, 2, and 3 weeks, respectively). The mean level for WT was set to 100%. Values are expressed with means \pm SEM. * $P < 0.05$, ** $P < 0.01$ significantly different from WT mice by Student's t test. (D) Reciprocal social interaction test after administration of DCS or saline (WT-saline, $n = 11$; WT-DCS, $n = 11$; 15q dup-saline, $n = 10$; 15q dup-DCS, $n = 12$). (E) Novelty-induced anxiety in open-field test after administration of DCS or saline (WT-saline, $n = 8$; WT-DCS, $n = 9$; 15q dup-saline, $n = 9$; 15q dup-DCS, $n = 10$). (F) Adult USV calls after administration of DCS or saline (WT-saline, $n = 8$; WT-DCS, $n = 9$; 15q dup-saline, $n = 9$; 15q dup-DCS, $n = 10$). Values are expressed with means \pm SEM. * $P < 0.05$, ** $P < 0.01$; N.S., not significant following Tukey-Kramer procedure.

group in the anterior CC compared with the WT-saline group (figs. S5 and S6). However, DCS did not normalize DMN connectivity between the frontal cortex and RSC (fig. S6).

Evoked BOLD responses to odor stimulation in the 15q dup-DCS group were observed in the ThN, hypothalamus, and somatosensory cortex (Fig. 6A). BOLD responses differed only marginally in the hypothalamus between 15q dup-DCS and 15q dup-saline groups (Fig. 6B) and did not significantly differ between WT-DCS and WT-saline groups. The total voxels that has the BOLD responses to odor stimulation was quantified by counting the number of suprathreshold (activated) voxels ($P < 0.05$, FDR-corrected at the cluster-wise level) comprising the activation map for each mouse. The total number of activated voxels in the 15q dup-saline group was substantially reduced relative to the WT-saline group (Fig. 6C). Moreover, the total number of activated voxels in the 15q dup-DCS group was increased compared to 15q dup-saline mice. This suggests that acute administration of DCS can lead to recovery of normal cortical activation to odor stimulation in 15q dup mice.

Modular brain network organization

Network modules are topographically distributed clusters of regions that are strongly connected with each other. Modules facilitate functional specialization and segregation of function. We identified modules in functional brain networks mapped in WT-saline, WT-DCS, 15q dup-saline, and 15q dup-DCS mice using a consensus partitioning based on the Louvain algorithm (28). This yielded a single group of modules representing a consensus across the four groups. Three distinct modules were identified. Fig. S7 (A and B) shows the three modules, namely, cortical network (module 1), subcortical network (module 2), and hindbrain-thalamic network (module 3). Most notably, administration of DCS in 15q dup mice resulted in increase of within-network connectivity strength in all modules (fig. S7C).

DISCUSSION

We developed an awake fMRI system for mice that does not necessitate anesthesia, thereby enabling us to investigate functional

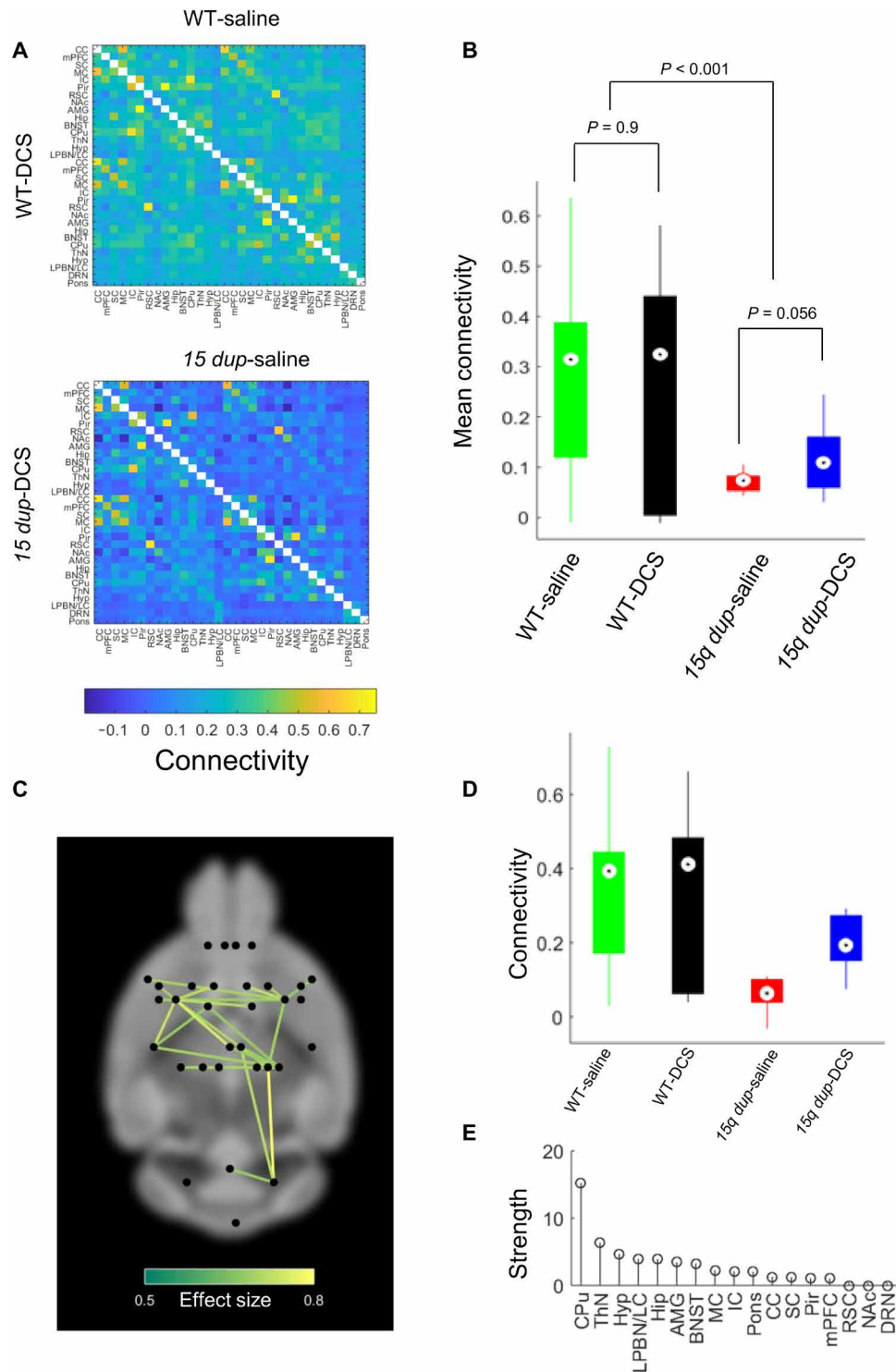


Fig. 5. Acute DCS treatment partially normalized rsfMRI functional connectivity in 15q dup mice. (A) Group-averaged connectivity matrices (Pearson correlation coefficients) for WT (top) and 15q dup (bottom) groups. Top right matrices show the group administered saline, and bottom left matrices show the group administered DCS. (B) Box plot comparing whole-brain-averaged (i.e., global) connectivity between WT and 15q dup groups administered saline or DCS. The P values indicated are for a two-sample t test performed on whole-brain-averaged connectivity. (C) Network of reduced connectivity in the 15q dup group identified with the NBS ($P < 0.01$). Connections are colored according to effect size (Cohen's d). (D) Box plot showing distribution of network-averaged connectivity in WT and 15q dup groups, stratified according to administration of DCS and saline. (E) Extent to which individual regions showed reversal of connectivity reductions following administration of DCS. Strength is the sum of effects sizes across all connections associated with a given region. Strength is averaged between contralateral regions.

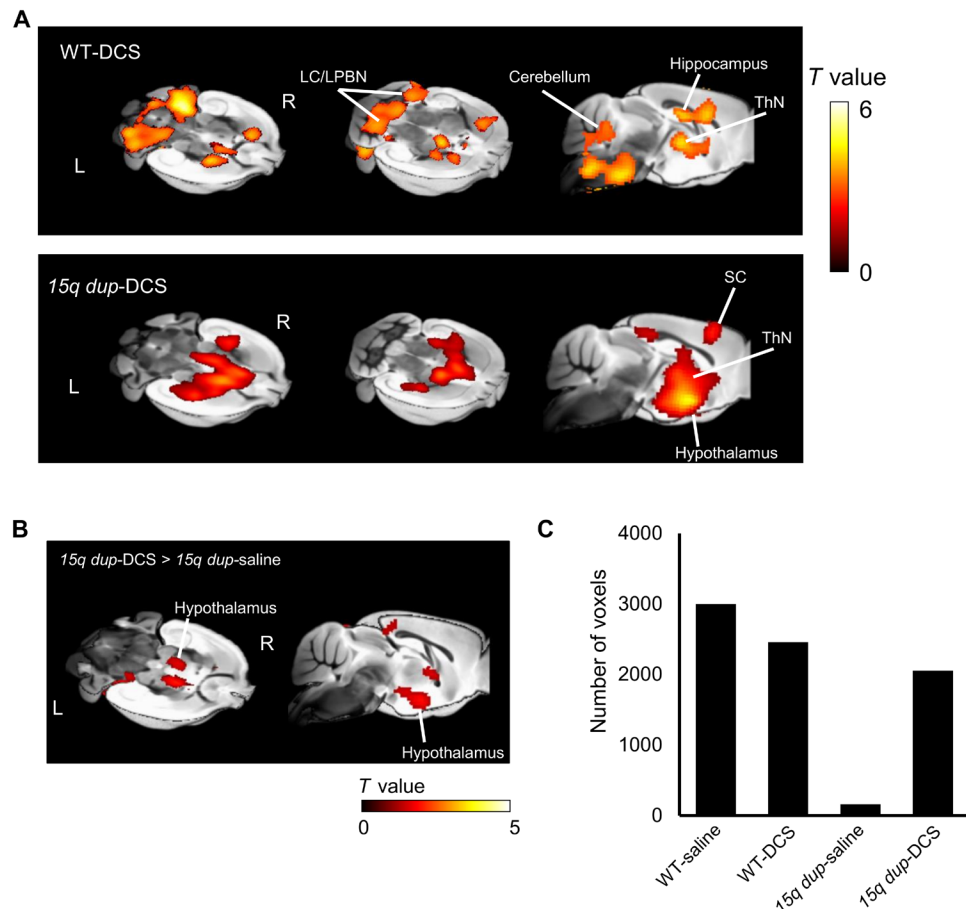


Fig. 6. Acute DCS treatment partially normalized odor fMRI response in *15q dup* mice. (A) Significant BOLD response to other-odor stimulation in *15q dup*-DCS ($n = 10$) and WT-DCS ($n = 10$) groups ($P < 0.05$, FDR-corrected at the cluster level). (B) Significant BOLD response to other-odor stimulation in *15q dup*-DCS compared to *15q dup*-saline ($P < 0.05$, FDR-corrected at the cluster level). (C) Total number of gray matter voxels with a significant BOLD response ($P < 0.05$, FDR-corrected at the cluster level) to other-odor stimulation.

brain connectivity and activation patterns in the conscious animal brain. Awake fMRI can bridge the gap between preclinical animal models and clinical human studies. Here, we demonstrated abnormal brain function in *15q dup* mice using two types of fMRI experiments: rsfMRI and task-based fMRI with an odor stimulation task. The first type enables mapping intrinsic regional interactions, which is an anatomically defined set of brain regions that preferentially activates during introspection and shows abnormal activity in psychiatric disorders (29–31). On the other hand, fMRI using the odor stimulation task provides utility in understanding the cognitive process related to social behavior. Furthermore, in combination with these techniques, we demonstrated that administration of DCS can rescue social behavior and normalize some functional connectivity alterations seen in the frontal cortex of *15q dup* mice. These results clearly demonstrate the utility of awake mouse fMRI.

Utility of awake fMRI to study brain function in mice

General anesthetics such as isoflurane and medetomidine are commonly used in animal fMRI studies to suppress intrascan body movement. However, anesthetics evoke vasoactive modulation of BOLD signals and markedly alter neuronal activity (32, 33). Whether anesthesia alters functional connectivity remains controversial. Previous study suggests that light anesthesia preserves patterns of functional connectivity in rodents

(34, 35); however, others show differences in functional connectivity between awake and anesthetized states. The total power of BOLD oscillations is reduced as a consequence of sedation (36). Light sedation can modify the BOLD response and local field potentials (37). Anesthesia clearly depresses consciousness, even if residual brain function is comparable to an awake state. In addition, it is impossible to perform cognitive tasks under anesthesia. Collectively, fMRI under anesthesia, even with light anesthesia, is not identical to fMRI in a conscious state, and thus, rodent fMRI performed with the animal anesthetized narrows opportunities to comprehensively characterize brain function and connectivity. For this reason, we developed an awake fMRI system for mice that does not necessitate anesthesia, thus enabling mouse fMRI experiments that were analogous to human fMRI.

We used a low dose of isoflurane before MRI acquisition to enable installation of the head immobilization apparatus and positioner. Isoflurane has dose-dependent side effects on the cardiovascular system, for example, decrease of voluntary respiration, blood pressure, and heart rate (33, 38). However, if the animals inhale a low dose of isoflurane over a relatively short interval (less than 10 min), then the animals can recover from these side effects within 10 min following cessation of isoflurane administration. A previous study reported that blood isoflurane was cleaned in 8 min (16). We verified that animals regained an awake state by showing that the power of gamma

band oscillations recorded from the frontal cortex significantly increased in 10 min following isoflurane cessation (fig. S2).

Despite these advantages, several factors complicate the implementation of awake mouse fMRI (39). To acquire high-quality fMRI data in awake mice, two of the most important considerations are suppression of the head motion and minimization of animal stress. We developed a customized head positioner to minimize head motion (figs. S1 and S3) and used robust motion correction methods, e.g., ICA-AROMA (Independent Component Analysis–Automatic Removal of Motion Artifacts) method (40) and framewise displacement (41), in addition to rigid body realignment. ICA-AROMA is one of the best performing head motion correction pipelines (42) and does not require additional regression of the head motion realignment parameters because they are accounted for as part of the pipeline. We verified that the extent of head immobilization achieved with our customized apparatus was sufficient to severely limit the potential for intrascan head movement (16). Recorded MRI noise was not presented to mice in first 2 days of acclimation training outside of MRI scanner to avoid multiple unfamiliar stresses at the same time. Our result showed that mice were stressed even with circumstance of fixed head, without MRI noise, at first day (fig. S1). Animal handling is critical to reduce animal stress. For example, tail handling is known to induce greater urination and defecation during handling, compared with using cupped hands to handle animals (43). Therefore, we used cupped hands to handle all animals and verified that by the last day of acclimation training, mice did not urinate during handling and rarely attempted to jump from the handler's cupped hands. Animal stress was further minimized with the use of mouse earplugs to reduce scanner noise and painless fixation of the head bar. With these advances and procedures, we were able to complete acclimation training in 4 days, which is comparable to the length of acclimation required in rat studies (18).

Previous studies have performed fMRI in awake rodents to assess responses to heat stimulation in TrpV1 knockout mice (44) and fear conditioned stimulation (16) and to investigate differences between awake and anesthetized states (14). Given that most genetically modified animals are mice, an integrated system to perform fMRI in awake mice is urgently required. This is the first study to demonstrate such a system and apply it to investigate altered brain function and connectivity in model mice of autism. We could provide important evidence for the utility of animal fMRI in future combination with other modalities, such as molecular biology, immunohistochemistry, and behavioral studies using circuit genetics.

Functional hypoconnectivity and disrupted FA in gray matter of *15q dup* mice

The *15q dup*-saline group showed widespread functional hypoconnectivity involving the entire cortex (Fig. 1A), which was most pronounced within the forebrain (Fig. 1B) relative to the WT-saline group. This accords with human fMRI studies in ASD reporting marked reductions in functional connectivity between the frontal lobes and the rest of the cortex (45). Human fMRI studies also indicate broad functional hyperconnectivity at the developmental stage of the disorder (46) and broad functional hypoconnectivity in adults (47). Functional connectivity abnormalities in ASD are therefore age dependent: hyperconnectivity in early development, followed by hypoconnectivity in adulthood. From a developmental perspective, the age of the mice studied here corresponds to early adulthood in humans. Regarding animal models, the phenotype and functional connectivity

differ markedly between types of transgenic mice. For example, *Fmr1*^{-/-} mice show robust hypoconnectivity (29, 48). Impaired prefrontal functional connectivity is a feature of other ASD mouse models (29–31). We previously showed that synaptic remodeling was altered at the developmental stage of *15q dup* mice (5), and this enhanced hyperconnectivity and local circuit stabilization might explain ASD pathology.

We also investigated FA in the gray matter of *15q dup* mice using DTI, a macroscopic technique enabling estimation of the orientation and organization of the projection of the white matter tracts. FA, a general measure indexing fiber density, axonal diameter, and myelination, showed widespread decreases in the *15q dup* group compared with the WT group. This provides a putative anatomical substrate for the observed functional hypoconnectivity, whereby aberrant formation of synapses and dendritic spines manifests as underfunctioning cortico-cortical connections in adulthood (49). This accords with the reduction in FA and functional hypoconnectivity that we observed and supports previous work reporting gray matter alterations in a complementary autism mouse model (23).

Odor perception

Human fMRI experiments investigating face perception indicate that neural responses to other faces are distinct between individuals with ASD and healthy individuals (50). This suggests a neural basis for altered interpersonal interactions in the disorder. Akin to the visual system in humans, the olfactory system in mice is crucial to recognizing other mice and memorizing objects (51). Thus, in mice, olfaction may be considered more important to interpersonal perception, kin recognition, and bond formation than vision. In this study, we therefore considered an odor perception fMRI task to assess odor perception deficits in our mouse model. We found that the region encompassing LC/LPBN, ThN, and hypothalamus was activated in response to odor stimulation in WT mice, but these activations were absent in *15q dup* mice (Fig. 2). The olfactory bulb was activated by odor stimulation both in WT and in *15q dup*-saline mice, indicating that *15q dup* mice show abnormalities in the processing of the odorant information rather than basic odor recognition and sensing functions supported by the olfactory bulb (fig. S4). In contrast to the olfactory bulb, we observed that *15q dup* mice showed a trend toward reduced activation in response to odor stimulation within the piriform cortex, compared to WT mice ($t = 2.0$ to 2.5). Given that habituation to the odorant stimulation reduces the BOLD response in higher-order olfactory regions, including the piriform cortex (52), future work should investigate this effect using alternative stimulation paradigms. Our previous positron emission tomography study using awake mice also showed decreased neural activity of DRN in *15q dup* mice (6). The LC and DRN interact bilaterally through serotonin [5-hydroxytryptamine (5-HT)], and the LC also has a noradrenergic projection to the cerebral cortex and ThN (53). Given that the *15q dup* mice show lower 5-HT levels than WT mice (4), the decrease of noradrenergic and serotonergic projections to the forebrain from the LC and the DRN may induce aberrant neuronal activity in the forebrain, including the cerebral cortex, ThN, and hypothalamus in *15q dup* mice.

Relationship between D/L-serine concentrations and ASD symptoms

We found that serine concentration was significantly reduced in the frontal cortices of *15q dup* mice. Functional hypoconnectivity was also most pronounced between frontal regions, and administration of

DCS partially normalized these deficits, including deficits associated with the medial prefrontal cortex (mPFC), and ameliorated abnormal social interactions. Notably, we found a relationship between severe hypoconnectivity between the mPFC and the insular cortex and significantly reduced D/L-serine concentrations in *15q dup* mice. Several positive effects of DCS on ASD individuals have been reported, including rescue of social function and amelioration of stereotypies (10). Supporting these clinical reports, DCS treatment affects ASD-like social or stereotypic behavior in some animal models of ASD (9). Because DCS binds to the glycine B site of NMDA receptors (NMDARs) as a coagonist and augments glutamate-mediated channel openings, the downstream effects of NMDARs are postulated to have a role in ASD etiology (54). Reduction of serine concentration in the *15q dup* mouse brain might cause abnormal social behavior mediated by hypo-NMDA function.

Limitations

A customized 30-mm-volume coil was engineered for the 4.7-T MRI system to accommodate the head bar. To compensate for the loss in signal-to-noise ratio owing to a relatively large coil diameter, we acquired fMRI images at a lower spatial resolution (0.2 mm × 0.2 mm × 1.0 mm), compared with previous studies using higher magnetic field strengths (13, 14, 27). Despite the loss in signal-to-noise ratio, our customized volume coil improved B1 homogeneity artifacts compared with more commonly used coils. Although our MRI system was adequate to demonstrate the utility of awake fMRI and test our hypotheses, future studies will undoubtedly benefit from higher-resolution acquisitions and stronger magnetic field strengths.

The advances and procedures that we used to minimize intrascan animal stress were verified on the basis of the monitoring of physiological measurements during acclimation training. However, we were unable to explicitly evaluate any potential residual effects of stress on the fMRI signal in this study. In addition, the impact of the stress during the acclimation training on the learned helplessness has not been assessed in this study. In the future, development of improved acclimation training protocols may further mitigate the potential effects of animal stress, while the use of commercial coils will improve fMRI quality.

Last, we were unable to establish odorant concentration during the other odor stimulation experiment. This was because the odor comprised multiple constituents. In future studies, consideration should be given to using a pure odorant or using alternative tasks that tap odor discrimination.

CONCLUSION

We demonstrated the utility of a novel system to perform fMRI in awake mice, without the need for any sedation or anesthesia. Using our system, we found that treatment with DCS normalizes functional hypoconnectivity in the frontal cortex of *15q dup* mice and rescues impaired social behavior that is characteristic of ASD. We also found that DCS normalizes odor-evoked cortical responses in the frontal cortex of *15q dup* mice. Given that awake fMRI can scan the “conscious” mouse brain during rest and task states, this advancement will enable not only fundamental studies aiming to link neural circuits with particular behaviors and functions but also preclinical studies aiming to understand the mechanisms of dysfunction and to probe the therapeutic action and efficacy of new treatments.

MATERIALS AND METHODS

Animals and surgery

The *15q dup* mice were bred for more than 10 generations on a C57BL/6J background, with duplication of the paternal allele (3). In all experiments, except for quantification of amino acids in juvenile mice, animal age ranged between 8 and 15 weeks, and animal weight ranged between 25 and 40 g. Only male mice were used. In MRI experiments, 25 WT (C57BL/6J) mice and 25 *15q dup* mice were allocated to the following groups: 15 WT-saline, 10 WT-DCS, 10 *15q dup*-saline, and 15 *15q dup*-DCS. In MRI experiments of olfactory bulb activation, 10 WT-DCS and 15 *15q dup*-DCS were used. The reciprocal social interaction test was conducted with 11, 11, 10, and 12 pairs of each genotype for WT-saline, WT-DCS, *15q dup*-saline, and *15q dup*-DCS, respectively. In the open-field test and USV analysis, 8 WT-saline, 9 WT-DCS, 9 *15q dup*-saline, and 10 *15q dup*-DCS were used. For quantification of free amino acid concentrations, six *15q dup* and six WT mice were used. To avoid food effects on the concentration of amino acids in this analysis, these mice were fasted during 9:00 to 15:00, after which brain tissues were extracted. For serine quantification in juvenile mice by HPLC, 4, 7, and 10 *15q dup* and 9, 6, and 7 WT mice of ages 1, 2, and 3 weeks, respectively, were used. For DTI analysis, 10 WT and 12 *15q dup* mice were used. The mice were housed individually in cages under controlled temperature conditions (23° ± 0.5°C) and a 12 hour:12 hour light-dark cycle (light on, 7:00; light off, 19:00) with free access to food and water. For serum corticosterone measurement, five (without MRI), four (training day 1), and five (training day 4) WT mice were used. For EEG recording, four WT mice were used. All animal experimental procedures in the present study were approved by the Institutional Review Board of Animal Ethical Committee who followed institutional guidelines in Ajinomoto Co. Inc. and the Ethics Committee of RIKEN.

Surgery for awake fMRI

For awake MRI experiments, we performed cranioplastic surgery on the mice under isoflurane anesthesia (1.5% with air), as previously described (fig. S1A) (44). Briefly, cranioplastic acrylic cement was mounted on the skull with a male plastic luer fitting (Male Luer Integral Lock Ring Plug Closed, Japan), which connected to a custom-made head positioner to fix the mouse's head during the MRI session without pain. After surgery, the mice were allowed to recover for more than a week.

fMRI acclimation training

During surgery recovery, mice were accustomed to the handling method (43). The handler lifted the mouse with cupped hands and held the animal for around 30 s. This handling continued for at least 1 week. We confirmed that mice did not urinate and did not jump from the cupped hands during handling. Then, mice were trained for 4 days to acclimatize to the awake fMRI conditions before fMRI experiments. They were trained at the same time each day (10:00 to 18:00) to minimize the effects of circadian rhythm variations. During the first 2 days, a pseudo-MRI system consisting of a nonmagnet bore and a head positioner was used. The mice were anesthetized by 2% isoflurane with air for induction and 1.5% with air for maintenance while positioning them on the MRI apparatus and adjusting the magnetic homogeneity, as described in the MRI section below. The mice were set on the head positioner by fixing the cranioplastic acrylic mount. To reduce possible stress induced by scanning noise, we used earplugs designed to fit the mouse's ears. The body was

gently wrapped with paper towel so that they can move freely within the paper towel cover. Mice remained in the pseudo-MRI apparatus for 30 min on the first day and 90 min on the second day. For the next 2 days, mice were placed in an MRI system under the same conditions (except for odor stimulation) as those used for the MRI measurements (fig. S1B). Throughout the training, heart and respiration rate were confirmed to be in the normal range using an MR-compatible monitoring system (model 1025; SA Instruments, Stony Brook, NY, USA).

fMRI procedure

We used a Bruker Avance III System (Bruker BioSpin, Ettlingen, Germany) with a 4.7-T/40-cm horizontal superconducting magnet with gradient coils (BGA12, 400 mT/m). A custom-made volume coil (30 mm in diameter) dedicated for the head positioner was used. The mice were anesthetized by 2% isoflurane with air for induction and less than 1.5% with air for maintenance while positioning them on the MRI apparatus and adjusting the magnetic homogeneity. Isoflurane was administered for no more than 10 min. The cranium of each mouse was then immediately immobilized in the dedicated volume coil by fixing the plastic luer fitting with a nonmagnetic stereotaxic apparatus. Magnetic field homogeneity was corrected using FASTMAP scout. Then, anesthesia was stopped to enable mice to awake. Mice awoke during the 10-min structural image scan. We confirmed that the respiration rate increased over 150 breaths/min following the 10-min recovery period. The fMRI acquisition then commenced. For odor stimulation, the odor was generated from the excretory products from stranger mice. In particular, excretory products were collected from three to five stranger mice. The stranger mice were isolated from the mice used for neuroimaging experiments. Excretory products were manually collected from the housing of the stranger mice after 1 week of housing and placed in the closed odorant box. The excretory products remained in the box for approximately 30 min before the MRI scan. At the commencement of scanning, the odorant box was connected to the odorant tube and air pump (Fig. 2A). An animal mask was used to deliver the odor to the nose of each mouse (Fig. 2B). The odor stimulation protocol contained five stimulation blocks, each of which comprised a 10-s period of odor delivery, followed by a 120-s rest block (Fig. 2C). During the “off” period, fresh air without any odor flowed to the mouse at the same rate as the flow of odor during the “on” period.

BOLD fMRI data were obtained using a T2*-weighted multislice echo planar imaging sequence with the following parameters: time of repetition, 2 s; echo time, 21 ms; field of view, 16 mm × 16 mm; acquisition matrix, 80 × 80 (200 μm × 200 μm/pixel); slice thickness, 1.0 mm; slice number, 15; number of volumes, 330 for resting state (11 min) and 345 for odor stimulation (11.5 min). While acquisition length is an important factor, we note that previous reports have successfully investigated functional connectivity using less than 300 volumes (14, 36). The slices were positioned including the mPFC and the cerebellum (+3 to −12 mm from the bregma). Because it was difficult to adjust the B0 field homogeneity in the whole brain, from the olfactory bulb to the cerebellum, we investigated the activation in the olfactory bulb separately. For olfactory bulb imaging, slice number is equal to 5 (+5 to 0 mm from the bregma). Structural images were obtained using a multislice rapid acquisition with a relaxation enhancement (RARE) sequence using the following parameters: time of repetition, 2500 ms; effective echo time, 60 ms; RARE factor, 8; acquisition matrix, 128 × 128; and four averages. To confirm that

acclimatization training minimized stress, the respiratory rate was measured during the training.

Diffusion tensor imaging

Diffusion tensor images were acquired from fixed brain tissue. First, mice were anesthetized with 2% isoflurane and then intracardially perfused with 30 ml of 0.1 M phosphate-buffered saline (PBS) containing heparin (1 U/ml), followed by 30 ml of 4% paraformaldehyde in PBS. After perfusion, whole brains were dissected and incubated in 4% paraformaldehyde in PBS overnight at 4°C. Subsequently, brains were washed with PBS and then incubated with PBS containing 2 mM ProHance and 0.02% sodium azide for 2 weeks. On the day before imaging, PBS was immersed to Fluorinert (FC-72, 3M) to equilibrate overnight at 4°C. Acquisition of DTI was conducted in the RIKEN Center for Brain Science in the support unit for Bio-Material Analysis in RIKEN Center for Brain Science, Research Resource Division. We used a 9.4-T Bruker Avance 400WB system (Bruker BioSpin, Ettlingen, Germany) with a volume coil of 15 mm in diameter. A spin echo sequence with the following parameters was used: time of repetition, 260 ms; echo time, 18 ms; field of view, 12 mm × 8 mm × 7 mm; acquisition matrix, 120 mm × 80 mm × 70 mm (100 μm × 100 μm × 100 μm/pixel); δ = 3 ms; Δ = 8 ms; number of segments, 4; total scan time, 100 min. Symmetric diffusion gradients were applied with $b = 1000 \text{ s/mm}^2$ in 30 noncollinear directions and $b = 0 \text{ s/mm}^2$ (A0 image) for the reference.

DCS injection

Intraperitoneal injection of DCS (Tokyo Chemical Industry, Tokyo, Japan) or saline (0.9% NaCl in distilled water) was administered to 15q dup mice. DCS was dissolved in saline. DCS (20 mg kg⁻¹ body weight) or saline was administered 30 min before behavioral testing and image acquisition, consistent with a recent report (9).

Data analysis

Preprocessing of images

SPM8 software (Wellcome Trust Center for Neuroimaging, UK) was used for preprocessing, including slice timing correction, motion correction by realignment, coregistration of the functional image to a structural brain image, and spatial normalization of the functional data. After head motion correction, the functional volumes were normalized to template image, which are coregistered to the mouse brain atlas (55), using the default nonlinear registration algorithm implemented in SPM8. The data were then processed using ICA-AROMA to correct for any remaining head movement (40).

Odor stimulation task-based fMRI

Following preprocessing, the normalized images were smoothed with a Gaussian filter [full width at half maximum (FWHM) = 0.6 mm]. Statistical analyses for odor stimulation were conducted using SPM8. The smoothed images were high pass-filtered for 100 s. The regressor was constructed by convolving the hemodynamic response function to the box-car model (on/off stimulation). Framewise displacement (41) was computed and regressed at the first-level analysis to control for head motion. A threshold of $P < 0.05$ (FDR-corrected at the cluster-wise level) was used to identify regional activation patterns associated with odor stimulation. To perform group inference, second-level (random effect) analyses were conducted by using the results of the first level analysis $P < 0.05$ (FDR-corrected at the cluster-wise level).

Resting-state functional connectivity

Frame-wise displacement (41) and time series derived from white matter, ventricles, and all gray matter were regressed because global signal is correlated with spontaneous, nonneuronal fluctuation of the blood flow. The residuals from this regression were used for all subsequent analyses. Detrending and bandpass filtering (0.01 to 0.1 Hz) were performed to exclude high-frequency components. Then, the processed images were smoothed with a Gaussian filter (FWHM = 0.6 mm). The Pearson correlation coefficient was computed between preprocessed and regionally averaged (32 regions) BOLD signals to yield a connectivity matrix for each mouse. The regions spanned the entire cortex and were drawn manually on the basis of the structural image corresponding to the mouse brain atlas (55). These 32 regions were selected on the basis of the regions related to the odor recognition and cognitive function.

Network-based statistic

The NBS (20) was used to identify functional connections (pairs of regions) that significantly differed in connectivity strength (Pearson correlation) between groups. We considered six independent comparisons among WT-saline, WT-DCS, *15q dup*-saline, *15q dup*-DCS. To correct for the three independent comparisons, a significance threshold of $\alpha = 0.05/6 = 0.008$ was enforced. For each comparison, a two-sample *t* test was performed independently for each distinct pair of regions (496 pairs) to test the null hypothesis of equality between groups in the mean Pearson correlation coefficient. This yielded a 32×32 matrix of *t* statistics. Connections with a *t* statistic threshold exceeding 3 were admitted to a suprathreshold graph, and connected components, referred to as subnetworks, were identified in this graph. The size of each subnetwork was measured as the number of suprathreshold connections that it comprised. To determine a familywise error-corrected *P* value for each subnetwork, permutation testing (5000 permutations) was used to generate a null distribution for the maximal subnetwork size. The *P* value for an observed subnetwork of the given size was estimated as the proportion of permutations for which the maximal subnetwork exceeded or equaled this size. To isolate subnetworks comprising the strongest effects, the *t* statistic threshold was increased from 3 to 6 in cases where widespread subnetworks were found for the lower threshold (Fig. 2B). The NBS provides control of the familywise error rate in the weak sense across the whole network; namely, the set of all connections. The *P* value associated with each subnetwork identified with the NBS was thus corrected for familywise errors across the whole network.

Modularity

Network modules were delineated in the 32×32 functional connectivity matrices constructed for each mouse. A consensus modular decomposition was also delineated for all mice (WT-saline, WT-DCS, *15q dup*-saline, and *15q dup*-DCS). The Louvain algorithm was used to identify modules, with the resolution parameter set to unity (56). To account for degeneracy in the solution space, the Louvain algorithm was implemented for 100 independent trials for each mouse, and a consensus matrix across these trials was generated. Because of the stochastic nature of the algorithm, decompositions varied across trials. Each cell in the consensus matrix stored the proportion of trials for which a given pair of regions belonged to a common module. Elements in the consensus matrix that were below a value of 0.4 were set to zero. The Louvain algorithm was applied to the thresholded matrix (100 trials) to yield a consensus modular decomposition (28). This process was iterated until the consensus matrices converged between successive iterations. To

determine a modular decomposition for all mice, a consensus matrix was first constructed across all mice, where each cell in this matrix stored the proportion of mice for which a given pair of nodes belonged to a common module. The Louvain algorithm was then applied to this consensus matrix. The modularity *Q* score (57) was used to quantify the extent to which each functional network was segregated into distinct modules. Higher *Q* scores indicate greater modular structure.

Dual-regression analysis

The REST toolkit (REST v1.8) and SPM8 were used to delineate the DMN. First, the preprocessed fMRI data were temporally detrended and bandpass-filtered (0.01 to 0.1 Hz). We used FMRIB Software Library (FSL) Multivariate Exploratory Linear Optimized Decomposition into Independent Components (MELODIC) for probabilistic ICA. The multisession temporal ICA concatenated approach was used for all mice in a temporally concatenated fashion for the ICA analysis. A total of 70 independent components were extracted from each analysis group (30, 58). Of the 70 independent components in each group, a representative network from a previous study was extracted, i.e., local cortical network, associated cortical network, sub-cortical network, limbic network, DMN, ThN, and cerebellum (fig. S5) (30, 48, 58). DMN was selected for comparison using dual regression. We used dual-regression program (FSL 5.0.2.2) for between-subject analysis, allowing for voxel-wise comparisons of rsfMRI data (30, 58). We used unpaired *t* tests to test for differences between groups.

FA map and structural connectivity in DTI

FA maps were calculated from the diffusion-weighted images using ParaVision 5.1 (Bruker BioSpin, Billerica, CA, USA). The FA maps were normalized to the template images using SPM 8. Normalization was performed via the T2 image ($b = 0 \text{ s/mm}^2$), which had a contrast that better resembled the template image than the FA maps. Regionally averaged FA values were determined for 18 gray matter regions by averaging FA values across all voxels comprising each region. FA values were compared between WT and *15q dup* groups using a two-way ANOVA.

Structural connectivity strength was quantified using two measures, mean FA and EW using DSI Studio software (<http://dsi-studio.labsolver.org>). FA at a given tracking point, measuring the degree of organization of the underlying white matter at each point, was computed and averaged over all tracked points on the fiber bundles. EW, which takes into account the number of fibers, the length of the fibers, and the ROI size, was computed as the following equation (59)

$$EW(i, j) = \frac{2}{S_i + S_j} \sum_{f \in F(i, j)} \frac{1}{L(f)}$$

where $F(i, j)$ is the set of fibers connecting ROIs i and j , S_i and S_j are the sizes of the two ROIs, f is each individual fiber within $F(i, j)$, and $L(f)$ is the length of fiber f .

Behavioral tests

Reciprocal social interaction test

Two mice with identical genotypes housed in different cages were placed in a box (50 cm \times 50 cm \times 50 cm; O'Hara & Co., Tokyo, Japan) with dim light (10 lux) and allowed to move freely for 10 min. These two mice not only had an identical genotype but also had the same age, sex, and similar body weight. In this test, a pair of mice was used as a sample. Images were captured at a rate of 2 per second by a charge-coupled device camera located above the field. An

interaction time was defined as any period of time in which the two mice either contacted each other or remained separated by no more than two body lengths. To avoid observer bias, interaction times were measured automatically using a custom macro for ImageJ.

Measurement of USV

A male mouse was placed in a soundproof box, and then, a female mouse was put in the cage. USVs emitted by the male were recorded by a condenser microphone (Avisoft, Berlin, Germany) for 5 min at a sampling rate of 250 kHz. Before the test day, each mouse was habituated in the field for 5 min without female exposure. Recorded data were analyzed by SASLab Pro (Avisoft). The number of calls was measured manually with single blinding.

Open-field test

The open-field test was performed with modified procedures reported in a previous study (4). Each mouse was permitted to freely move in the open-field apparatus (50 cm × 50 cm × 50 cm). Total distance traveled, vertical activity (rearing measured by counting the number of photobeam interruptions), and time spent in the center area of open-field were recorded for 60 min by using TimeOF (O'Hara & Co.), which allows automated measurements.

Quantification of free amino acid concentrations in brain tissues

Six *15q dup* mice and six littermate mice (WT) were euthanized under anesthesia at fasting diurnal phase (9:00 to 15:00). Tissue from seven regions (cerebellum, hippocampus, hypothalamus, midbrain, olfactory bulb, frontal cortex, and pons/medulla) was collected in ice-cold PBS to quench the enzymatic reaction, quickly frozen in liquid nitrogen, then stored at -80°C . Free amino acid concentrations in these samples were measured by LC-MS/MS analysis, using a protocol modified from a previous study (60). The frozen tissue of each brain region was homogenized using Multi-beads shocker (Yasui Kikai, Osaka, Japan) in an ice-cold 80% MeOH aqueous solution containing L-phenylalanine-*d*5 as the internal standard (to correct the extraction of amino acids from tissues) at a concentration of 10-mg wet tissue/ml. The homogenate (500 μl) was further mixed with 500 μl of water and 500 μl of chloroform and then centrifuged at 15,000 rpm for 5 min at 4°C . A portion of this supernatant (600 μl) was transferred to a sample tube, dried under reduced pressure, and then redissolved in 60 μl of water. The amino acids in the samples were derivatized with the 3-aminopyridyl-*N*-hydroxysuccinimidyl carbamate (APDS) as follows. The sample solution (10 μl) from the tissues was dissolved in 60 μl of 200 mM sodium borate buffer (pH 8.8), and then, 20 μl of APDS (10 mg/ml) in acetonitrile was added and heated at 55°C for 10 min. An aqueous 0.1% (v/v) formic acid solution (100 μl) and 25 mM formic acid (pH 6.0, adjusted with aqueous ammonium) solution (300 μl) were then added, and 1 μl of the reaction mixture was subjected to LC-MS/MS. Inertsil C8-3 column (2.1 mm by 100 mm, GL Sciences, Tokyo, Japan) was used for the separation, and the mobile phase was consisted of eluent A (25 mM ammonium formate in water) and eluent B (water:acetonitrile = 40:60). The amino acids were separated by an Agilent 1100 series LC system (Agilent Technologies, Waldbrunn, Germany) and analyzed with AB Sciex API 4000. The AB Sciex Analyst 1.4.2 software was used to control these instruments and quantitate each amino acid.

Serine quantification in brain tissues

The concentration of L- and D-serine in brain tissues was measured by HPLC analysis. Frontal cerebral cortex was dissected and homog-

enized in 0.2 M ice-cold perchloric acid. The homogenates were cooled on ice for 30 min to deproteinize and centrifuged at 20,000g for 15 min at 0°C . The supernatant was filtered through a 0.45- μm filter (Merck Millipore, Darmstadt, Germany), and then, L- and D-serine were measured with HPLC system (HTEC-500; Eicom, Kyoto, Japan). Precolumn derivatization was performed with 4 mM *o*-phthaldialdehyde/*N*-acetyl-L-cystein (pH 10.0) in an autosampling injector system (M-500; Eicom) at 10°C for 5 min. The derivatives were separated in the octadecylsilane column (EX-3ODS, ϕ 4.6 mm by 100 mm long; Eicom) at 30°C with 0.1 M PBS (pH 6.0) containing 18% methanol. The HPLC system was set to an applied potential of +600 mV versus an Ag/AgCl reference analytical electrode. The amount of serine was determined with peak area using PowerChrom (ϵ DAQ, NSW, Australia) with external standards (Sigma-Aldrich). Values were normalized by tissue weight.

Serum corticosterone levels

Blood was collected after the training. To serve as a control condition, blood was also acquired in mice that had not been subjected to training. Immediately following decapitation, trunk blood was collected, and blood samples were immediately placed on ice. The plasma was collected after centrifuging samples at 1800g for 15 min at 4°C . The plasma was stored at -80°C until assayed in duplicate using a corticosterone enzyme-linked immunosorbent assay kit (Enzo Life Sciences, Farmingdale, NY, USA) following manufacturer's instructions.

EEG

Surgery

Mice were anesthetized with 1.5% isoflurane, and the stainless steel screws (1000 μm in diameter) were implanted into the skull overlying the frontal cortex (AP, -0.5 mm; ML, -0.5 mm from the bregma). A reference stainless steel screw was implanted into the skull in the hindbrain (AP, -6 mm; ML, -0.5 mm from the bregma). Once two screws were implanted, dental cement (GC Unifast Trad; GC Co., Tokyo, Japan) and an adhesive (Super-Bond C&B, Sun Medical Co. LTD., Shiga, Japan) were applied around the shaft of the screws and over the exposed skull.

EEG recording

Following recovery from the surgery, mice were anesthetized with the same protocol as fMRI experiments. Electrodes were immediately connected to a differential AC amplifier Model 1700 (A-M Systems, Sequim, WA, USA), via a Model 1700 head stage (A-M Systems, Sequim, WA, USA). Local field potentials (LFP) were continuously recorded. EEG signals in the frontal cortex were acquired at a 10-kHz sampling rate using dedicated data acquisition software (PowerLab, ADInstruments, Dunedin, New Zealand). After the recording with 1.5% isoflurane anesthesia for 10 min, isoflurane was turned off, and the recording was continued until 10 min. The body temperature was maintained at 37°C using a heating pad (DC temperature controller; FHC Inc., Bowdoin, ME, USA). From EEG signal, the averaged power of gamma frequency band (60 to 100 Hz) during the isoflurane anesthesia and 9 to 10 min after turning off the isoflurane was calculated.

SUPPLEMENTARY MATERIALS

Supplementary material for this article is available at <http://advances.sciencemag.org/cgi/content/full/6/6/eaav4520/DC1>

Fig. S1. Awake fMRI system and physiological parameters.

Fig. S2. EEG recording.

Fig. S3. Head motion parameters.

Fig. S4. Similar BOLD response to odor stimulation in the olfactory bulb between WT and *15q dup*-saline mice.

Fig. S5. Common ICA components in WT and *15q dup* mice.

Fig. S6. DMN in WT and *15q dup* mice.

Fig. S7. Modular decomposition of functional connectivity networks and comparison of within-module-averaged connectivity.

Table S1. Amino acid concentration in hindbrain in WT and *15q dup* mice.

Table S2. Amino acid concentration in forebrain in WT and *15q dup* mice.

REFERENCES AND NOTES

1. T. Takumi, K. Tamada, F. Hatanaka, N. Nakai, P. F. Bolton, Behavioral neuroscience of autism. *Neurosci. Biobehav. Rev.* **2019**, S0149-7634(18)30372-5 (2019).
2. T. Takumi, K. Tamada, CNV biology in neurodevelopmental disorders. *Curr. Opin. Neurobiol.* **48**, 183–192 (2018).
3. J. Nakatani, K. Tamada, F. Hatanaka, S. Ise, H. Ohta, K. Inoue, S. Tomonaga, Y. Watanabe, Y. J. Chung, R. Banerjee, K. Iwamoto, T. Kato, M. Okazawa, K. Yamauchi, K. Tanda, K. Takao, T. Miyakawa, A. Bradley, T. Takumi, Abnormal behavior in a chromosome-engineered mouse model for human 15q11-13 duplication seen in autism. *Cell* **137**, 1235–1246 (2009).
4. K. Tamada, S. Tomonaga, F. Hatanaka, N. Nakai, K. Takao, T. Miyakawa, J. Nakatani, T. Takumi, Decreased exploratory activity in a mouse model of 15q duplication syndrome: implications for disturbance of serotonin signaling. *PLOS ONE* **5**, e15126 (2010).
5. M. Isshiki, S. Tanaka, T. Kuriu, K. Tabuchi, T. Takumi, S. Okabe, Enhanced synapse remodelling as a common phenotype in mouse models of autism. *Nat. Commun.* **5**, 4742 (2014).
6. N. Nakai, M. Nagano, F. Saitow, Y. Watanabe, Y. Kawamura, A. Kawamoto, K. Tamada, H. Mizuma, H. Onoe, Y. Watanabe, H. Monai, H. Hirase, J. Nakatani, H. Inagaki, T. Kawada, T. Miyazaki, M. Watanabe, Y. Sato, S. Okabe, K. Kitamura, M. Kano, K. Hashimoto, H. Suzuki, T. Takumi, Serotonin rebalances cortical tuning and behavior linked to autism symptoms in 15q11-13 CNV mice. *Sci. Adv.* **3**, e1603001 (2017).
7. C. Piochon, A. D. Kloth, G. Grasselli, H. K. Titley, H. Nakayama, K. Hashimoto, V. Wan, D. H. Simmons, T. Eissa, J. Nakatani, A. Cherskov, T. Miyazaki, M. Watanabe, T. Takumi, M. Kano, S. S.-H. Wang, C. Hansel, Cerebellar plasticity and motor learning deficits in a copy-number variation mouse model of autism. *Nat. Commun.* **5**, 5586 (2014).
8. J. Ellegood, E. Anagnostou, B. A. Babineau, J. N. Crawley, L. Lin, M. Gestine, E. DiCicco-Bloom, J. K. Lai, J. A. Foster, O. Peñagarikano, D. H. Geschwind, L. K. Pacey, D. R. Hampson, C. L. Laliberté, A. A. Mills, E. Tam, L. R. Osborne, M. Kouser, F. Espinosa-Becerra, Z. Xuan, C. M. Powell, A. Raznahan, D. M. Robins, N. Nakai, J. Nakatani, T. Takumi, M. C. van Eede, T. M. Kerr, C. Muller, R. D. Blakely, J. Veenstra-VanderWeele, R. M. Henkelman, J. P. Lerch, Clustering autism: Using neuroanatomical differences in 26 mouse models to gain insight into the heterogeneity. *Mol. Psychiatry* **20**, 118–125 (2015).
9. T.-N. Huang, H.-C. Chuang, W.-H. Chou, C.-Y. Chen, H.-F. Wang, S.-J. Chou, Y.-P. Hsueh, Tbr1 haploinsufficiency impairs amygdalar axonal projections and results in cognitive abnormality. *Nat. Neurosci.* **17**, 240–247 (2014).
10. N. F. Minshawi, L. K. Wink, R. Shaffer, M. H. Plawecki, D. J. Posey, H. Liu, S. Hurwitz, C. J. McDougle, N. B. Swiezy, C. A. Erickson, A randomized, placebo-controlled trial of D-cycloserine for the enhancement of social skills training in autism spectrum disorders. *Mol. Autism* **7**, 2 (2016).
11. J. Grandjean, A. Schroeter, I. Batata, M. Rudin, Optimization of anesthesia protocol for resting-state fMRI in mice based on differential effects of anesthetics on functional connectivity patterns. *Neuroimage* **102**, 838–847 (2014).
12. Q. Bukhari, A. Schroeter, D. M. Cole, M. Rudin, Resting state fMRI in mice reveals anesthesia specific signatures of brain functional networks and their interactions. *Front. Neural Circuits* **11**, 5 (2017).
13. M. Desai, I. Kahn, U. Knoblich, J. Bernstein, H. Atallah, A. Yang, N. Kopell, R. L. Buckner, A. M. Graybiel, C. I. Moore, E. S. Boyden, Mapping brain networks in awake mice using combined optical neural control and fMRI. *J. Neurophysiol.* **105**, 1393–1405 (2011).
14. K. Yoshida, Y. Mimura, R. Ishihara, H. Nishida, Y. Komaki, T. Minakuchi, T. Tsurugizawa, M. Mimura, H. Okano, K. F. Tanaka, N. Takata, Physiological effects of a habituation procedure for functional MRI in awake mice using a cryogenic radiofrequency probe. *J. Neurosci. Methods* **274**, 38–48 (2016).
15. D. Madularu, A. P. Mathieu, C. Kumaragamage, L. M. Reynolds, J. Near, C. Flores, M. N. Rajah, A non-invasive restraining system for awake mouse imaging. *J. Neurosci. Methods* **287**, 53–57 (2017).
16. A. P. Harris, R. J. Lennen, I. Marshall, M. A. Jansen, C. R. Pernet, N. M. Brydges, I. C. Duguid, M. C. Holmes, Imaging learned fear circuitry in awake mice using fMRI. *Eur. J. Neurosci.* **42**, 2125–2134 (2015).
17. A. Uematsu, A. Kitamura, K. Iwatsuki, H. Uneyama, T. Tsurugizawa, Correlation between activation of the prelimbic cortex, basolateral amygdala, and agranular insular cortex during taste memory formation. *Cereb. Cortex* **25**, 2719–2728 (2015).
18. P. Stenroos, J. Paasonen, R. A. Salo, K. Jokivarsi, A. Shatillo, H. Tanila, O. Gröhn, Awake rat brain functional magnetic resonance imaging using standard radio frequency coils and a 3D printed restraint kit. *Front. Neurosci.* **12**, 548 (2018).
19. J. Kortelainen, X. Jia, T. Seppänen, N. Thakor, Increased electroencephalographic gamma activity reveals awakening from isoflurane anaesthesia in rats. *Br. J. Anaesth.* **109**, 782–789 (2012).
20. A. Zalesky, A. Fornito, E. T. Bullmore, Network-based statistic: Identifying differences in brain networks. *Neuroimage* **53**, 1197–1207 (2010).
21. A. J. Poplawsky, M. Fukuda, M. Murphy, S.-G. Kim, Layer-specific fMRI responses to excitatory and inhibitory neuronal activities in the olfactory bulb. *J. Neurosci.* **35**, 15263–15275 (2015).
22. A. Pfefferbaum, E. Adalsteinsson, T. Rohlfing, E. V. Sullivan, Diffusion tensor imaging of deep gray matter brain structures: Effects of age and iron concentration. *Neurobiol. Aging* **31**, 482–493 (2010).
23. M. Kumar, S. Kim, S. Pickup, R. Chen, A. H. Fairless, R. Ittyerah, T. Abel, E. S. Brodtkin, H. Poptani, Longitudinal in-vivo diffusion tensor imaging for assessing brain developmental changes in BALB/cJ mice, a model of reduced sociability relevant to autism. *Brain Res.* **1455**, 56–67 (2012).
24. B. B. Bendlin, M. L. Ries, M. Lazar, A. L. Alexander, R. J. Dempsey, H. A. Rowley, J. E. Sherman, S. C. Johnson, Longitudinal changes in patients with traumatic brain injury assessed with diffusion-tensor and volumetric imaging. *Neuroimage* **42**, 503–514 (2008).
25. F. L. Margolis, Carnosine in the primary olfactory pathway. *Science* **184**, 909–911 (1974).
26. H. Lu, Q. Zou, H. Gu, M. E. Raichle, E. A. Stein, Y. Yang, Rat brains also have a default mode network. *Proc. Natl. Acad. Sci. U.S.A.* **109**, 3979–3984 (2012).
27. J. Grandjean, V. Zerbi, J. H. Balsters, N. Wenderoth, M. Rudin, Structural basis of large-scale functional connectivity in the mouse. *J. Neurosci.* **37**, 8092–8101 (2017).
28. A. Lancichinetti, S. Fortunato, Consensus clustering in complex networks. *Sci. Rep.* **2**, 336 (2012).
29. M. G. Haberl, V. Zerbi, A. Veltien, M. Ginger, A. Heerschap, A. Frick, Structural-functional connectivity deficits of neocortical circuits in the Fmr1^{-/-} mouse model of autism. *Sci. Adv.* **1**, e1500775 (2015).
30. V. Zerbi, G. D. Ielacqua, M. Markicevic, M. G. Haberl, M. H. Ellisman, A. A-Bhaskaran, A. Frick, M. Rudin, N. Wenderoth, Dysfunctional autism risk genes cause circuit-specific connectivity deficits with distinct developmental trajectories. *Cereb. Cortex* **28**, 2495–2506 (2018).
31. A. Bertero, A. Liska, M. Pagani, R. Parolisi, M. E. Masferrer, M. Gritti, M. Pedrazzoli, A. Galbusera, A. Sarica, A. Cerasa, M. Buffelli, R. Tonini, A. Buffo, C. Gross, M. Pasqualetti, A. Gozzi, Autism-associated 16p11.2 microdeletion impairs prefrontal functional connectivity in mouse and human. *Brain* **141**, 2055–2065 (2018).
32. M. T. Alkire, J. Miller, General anesthesia and the neural correlates of consciousness. *Prog. Brain Res.* **150**, 229–244 (2005).
33. T. Tsurugizawa, Y. Takahashi, F. Kato, Distinct effects of isoflurane on basal BOLD signals in tissue/vascular microstructures in rats. *Sci. Rep.* **6**, 38977 (2016).
34. J. Grandjean, A. Corcobá, M. C. Kahn, A. L. Upton, E. S. Deneris, E. Seifritz, F. Helmchen, E. O. Mann, M. Rudin, B. J. Saab, A brain-wide functional map of the serotonergic responses to acute stress and fluoxetine. *Nat. Commun.* **10**, 350 (2019).
35. Y. Zhan, R. C. Paolicelli, F. Sforzini, L. Weinhard, G. Bolasco, F. Pagani, A. L. Vyssotski, A. Bifone, A. Gozzi, D. Ragozzino, C. T. Gross, Deficient neuron-microglia signaling results in impaired functional brain connectivity and social behavior. *Nat. Neurosci.* **17**, 400–406 (2014).
36. J. Paasonen, P. Stenroos, R. A. Salo, V. Kiviniemi, O. Gröhn, Functional connectivity under six anesthesia protocols and the awake condition in rat brain. *Neuroimage* **172**, 9–20 (2018).
37. T. Tsurugizawa, L. Ciobanu, D. Le Bihan, Water diffusion in brain cortex closely tracks underlying neuronal activity. *Proc. Natl. Acad. Sci. U.S.A.* **110**, 11636–11641 (2013).
38. C. Constantinides, S. Angeli, R. Mean, Murine cardiac hemodynamics following manganese administration under isoflurane anesthesia. *Ann. Biomed. Eng.* **39**, 2706–2720 (2011).
39. C. F. Ferris, B. Smerkers, P. Kulkarni, M. Caffrey, O. Afacan, S. Toddes, T. Stolberg, M. Febo, Functional magnetic resonance imaging in awake animals. *Rev. Neurosci.* **22**, 665–674 (2011).
40. R. H. R. Pruij, M. Mennes, D. van Rooij, A. Llera, J. K. Buitelaar, C. F. Beckmann, ICA-AROMA: A robust ICA-based strategy for removing motion artifacts from fMRI data. *Neuroimage* **112**, 267–277 (2015).
41. J. D. Power, K. A. Barnes, A. Z. Snyder, B. L. Schlaggar, S. E. Petersen, Spurious but systematic correlations in functional connectivity MRI networks arise from subject motion. *Neuroimage* **59**, 2142–2154 (2012).
42. L. Parkes, B. Fulcher, M. Yücel, A. Fornito, An evaluation of the efficacy, reliability, and sensitivity of motion correction strategies for resting-state functional MRI. *Neuroimage* **171**, 415–436 (2018).
43. J. L. Hurst, R. S. West, Taming anxiety in laboratory mice. *Nat. Methods* **7**, 825–826 (2010).

44. T. Tsurugizawa, Y. Nogusa, Y. Ando, H. Uneyama, Different TRPV1-mediated brain responses to intragastric infusion of capsaicin and capsiate. *Eur. J. Neurosci.* **38**, 3628–3635 (2013).
45. M. Murias, S. J. Webb, J. Greenson, G. Dawson, Resting state cortical connectivity reflected in EEG coherence in individuals with autism. *Biol. Psychiatry* **62**, 270–273 (2007).
46. K. Supekar, L. Q. Uddin, A. Khouzam, J. Phillips, W. D. Gaillard, L. E. Kenworthy, B. E. Yerys, C. J. Vaidya, V. Menon, Brain hyperconnectivity in children with autism and its links to social deficits. *Cell Rep.* **5**, 738–747 (2013).
47. S. Ha, I.-J. Sohn, N. Kim, H. J. Sim, K.-A. Cheon, Characteristics of brains in autism spectrum disorder: Structure, function and connectivity across the lifespan. *Exp. Neurobiol.* **24**, 273–284 (2015).
48. V. Zerbi, J. Grandjean, M. Rudin, N. Wenderoth, Mapping the mouse brain with rs-fMRI: An optimized pipeline for functional network identification. *Neuroimage* **123**, 11–21 (2015).
49. P. Penzes, M. E. Cahill, K. A. Jones, J.-E. VanLeeuwen, K. M. Woolfrey, Dendritic spine pathology in neuropsychiatric disorders. *Nat. Neurosci.* **14**, 285–293 (2011).
50. K. Pierce, R.-A. Müller, J. Ambrose, G. Allen, E. Courchesne, Face processing occurs outside the fusiform 'face area' in autism: Evidence from functional MRI. *Brain* **124**, 2059–2073 (2001).
51. K. Richter, G. Wolf, M. Engelmann, Social recognition memory requires two stages of protein synthesis in mice. *Learn. Mem.* **12**, 407–413 (2005).
52. F. Zhao, X. Wang, H. A. Zariwala, J. M. Uslaner, A. K. Houghton, J. L. Evelhoch, D. S. Williams, C. T. Winkelmann, fMRI study of olfaction in the olfactory bulb and high olfactory structures of rats: Insight into their roles in habituation. *Neuroimage* **127**, 445–455 (2016).
53. E. R. Samuels, E. Szabadi, Functional neuroanatomy of the noradrenergic locus coeruleus: Its roles in the regulation of arousal and autonomic function part II: Physiological and pharmacological manipulations and pathological alterations of locus coeruleus activity in humans. *Curr. Neuropharmacol.* **6**, 254–285 (2008).
54. E.-J. Lee, S. Y. Choi, E. Kim, NMDA receptor dysfunction in autism spectrum disorders. *Curr. Opin. Pharmacol.* **20**, 8–13 (2015).
55. B. J. K. P. Franklin, G. Paxinos, in *The Mouse Brain In Stereotaxic Coordinates* (Elsevier, ed. 3, 2007).
56. B. Biswal, F. Z. Yetkin, V. M. Haughton, J. S. Hyde, Functional connectivity in the motor cortex of resting human brain using echo-planar MRI. *Magn. Reson. Med.* **34**, 537–541 (1995).
57. M. E. Newman, Modularity and community structure in networks. *Proc. Natl. Acad. Sci. U.S.A.* **103**, 8577–8582 (2006).
58. J. Grandjean, D. Azzinnari, A. Seuwen, H. Sigrist, E. Seifritz, C. R. Pryce, M. Rudin, Chronic psychosocial stress in mice leads to changes in brain functional connectivity and metabolite levels comparable to human depression. *Neuroimage* **142**, 544–552 (2016).
59. P. Hagmann, L. Cammoun, X. Gigandet, R. Meuli, C. J. Honey, V. J. Wedeen, O. Sporns, Mapping the structural core of human cerebral cortex. *PLOS Biol.* **6**, e159 (2008).
60. K. Shimbo, T. Oonuki, A. Yahashi, K. Hirayama, H. Miyano, Precolumn derivatization reagents for high-speed analysis of amines and amino acids in biological fluid using liquid chromatography/electrospray ionization tandem mass spectrometry. *Rapid Commun. Mass Spectrom.* **23**, 1483–1492 (2009).

Acknowledgments: We are grateful to F. Kato (The Jikei University School of Medicine), E. Kuwazawa, and T. Tokita (Animal Support Kobe, Kobe, Japan) for technical assistance with the MRI measurements, and we thank K. Torii (Torii Nutrient-State Institute Inc.) for valuable comments for this study. **Funding:** This work was funded by Ajinomoto Co. Inc.; KAKENHI Grant-in-Aid for Young Scientists, Scientific Research (S), and Scientific Research on Innovative Areas (16H06316, 16H06463, and 24700380); JST CREST; and the Takeda Science Foundation and Smoking Science Foundation. A.Z. was supported by the Australian National Health and Medical Research Council (NHMRC) Senior Research Fellowship B (ID: 1136649). **Author contributions:** T.Ts., K.T., and T.Ta. designed the experiments. T.Ts., A.K., and J.H. performed the MRI experiments. T.Ts., C.D., and A.Z. analyzed the MRI data. K.T. performed behavior tests and serine quantification. N.O., S.K., and Y.K. measured the free amino acid concentrations. H.O. supported MRI experiments at RIKEN. T.Ts., K.T., A.K., A.Z., and T.Ta. wrote the manuscript. **Competing interests:** The authors declare that they have no competing interests. **Data and materials availability:** All data needed to evaluate the conclusions in the paper are present in the paper and/or the Supplementary Materials. Additional data related to this paper may be requested from the authors.

Submitted 17 September 2018

Accepted 22 November 2019

Published 5 February 2020

10.1126/sciadv.aav4520

Citation: T. Tsurugizawa, K. Tamada, N. Ono, S. Karakawa, Y. Kodama, C. Debacker, J. Hata, H. Okano, A. Kitamura, A. Zalesky, T. Takumi, Awake functional MRI detects neural circuit dysfunction in a mouse model of autism. *Sci. Adv.* **6**, eaav4520 (2020).